Exponential Gain and Saturation of a Self-Amplified Spontaneous Emission Free-Electron Laser

S. V. Milton,[1]* E. Gluskin,[1] N. D. Arnold,[1] C. Benson,[1] W. Berg,[1] S. G. Biedron,[1,2] M. Borland,[1] Y.-C. Chae,[1] R. J. Dejus,[1] P. K. Den Hartog,[1] B. Deriy,[1] M. Erdmann,[1] Y. I. Eidelman,[1] M. W. Hahne,[1] Z. Huang,[1] K.-J. Kim,[1] J. W. Lewellen,[1] Y. Li,[1] A. H. Lumpkin,[1] O. Makarov,[1] E. R. Moog,[1] A. Nassiri,[1] V. Sajaev,[1] R. Soliday,[1] B. J. Tieman,[1] E. M. Trakhtenberg,[1] G. Travish,[1] I. B. Vasserman,[1] N. A. Vinokurov,[3] X. J. Wang, G. Wiemerslage,[1] B. X. Yang[1]

Self-amplified spontaneous emission in a free-electron laser has been proposed for the generation of very high brightness coherent x-rays. This process involves passing a high-energy, high-charge, short-pulse, low-energy-spread, and low-emittance electron beam through the periodic magnetic field of a long series of high-quality undulator magnets. The radiation produced grows exponentially in intensity until it reaches a saturation point. We report on the demonstration of self-amplified spontaneous emission gain, exponential growth, and saturation at visible (530 nanometers) and ultraviolet (385 nanometers) wavelengths. Good agreement between theory and simulation indicates that scaling to much shorter wavelengths may be possible. These results confirm the physics behind the self-amplified spontaneous emission process and forward the development of an operational x-ray free-electron laser.

Generation of high-brightness (photon flux per frequency bandwidth per unit phase space volume) hard x-rays (photon energies greater than ~5 keV or wavelengths less than 2.5 Å) has long been the domain of synchrotron light sources based on high-energy electron storage rings (*1–3*). However, important advances in x-ray brightness could potentially be achieved by using free-electron lasing action at these short wavelengths. Unfortunately, free-electron lasers (FELs) based on the oscillator principle and conventional laser systems are limited on the short-wavelength side to ultraviolet wavelengths, primarily because of mirror or seed beam limitations.

Free-electron lasing at wavelengths shorter than ultraviolet and including hard x-rays can be achieved with a single-pass, high-gain FEL based on the self-amplified spontaneous emission (SASE) process (*4–8*). A high-quality, high-peak-current electron beam is accelerated and passed through an undulator (a long, high-quality, sinusoidally varying magnetic field). A favorable instability begins between the electron beam and the electromagnetic (EM) wave it is producing, and the optical power increases exponentially until the process eventually saturates at some maximum radiation output level. At x-ray wavelengths, the peak brightness would be much higher (by more than 10 orders of magnitude) than the brightness of sources available today at comparable wavelengths.

Another important feature is that this process can occur at any wavelength because it scales with the electron beam energy and so is continuously tunable in wavelength. Achieving saturation of the process is thus a matter of providing an undulator of sufficient length and quality and then passing a sufficiently high energy, high quality beam through the undulator field.

Measurements of the SASE process operating to saturation have been previously made; however, none were at wavelengths shorter than 585×10^3 nm (*9*). As a direct result of advances in the areas of high-brightness electron beam production with photocathode radio-frequency (rf) electron guns (*10, 11*) and long, high-quality undulator magnets such as those now used at all major synchrotron light source facilities, recent progress has been made at extending the measurements of the SASE process to shorter wavelengths (*12–14*) [in one case, to a wavelength of 80 nm (*15*)].

Our low-energy undulator test line (LEUTL) (Fig. 1) and its various component systems (*16–23*) are designed to achieve and explore the SASE FEL process to saturation in the visible and ultraviolet wavelengths and to explore topics of interest for a next-generation linac-based light source. With a frequency-quadrupled Nd:glass drive laser, high-quality electron bunches are generated via the photoelectric effect within a photocathode rf gun using copper as the cathode material. The electron bunch is initially accelerated to ~5 MeV, then injected into the linear accelerator, and further accelerated to the desired energy (up to a maximum of 650 MeV). In addition to acceleration, the beam undergoes magnetic bunch compression to increase the peak current. Finally, it is passed through the undulator field, where SASE begins.

The essence of SASE lies in the generation of EM radiation by the electrons as they are transversely accelerated by the magnetic field of the undulator magnet and by the interaction of the EM field back on the electrons. When an electron beam traverses an undulator, it emits EM radiation at the resonant wavelength $\lambda_r = (\lambda_u/2\gamma^2)(1 + K^2/2)$. Here, λ_u is the undulator period, γmc^2 is the electron beam energy, $K = eB_o\lambda_u/2\pi mc$ is the dimensionless undulator strength parameter, and B_o is the maximum on-axis magnetic field strength of the undulator. Although the EM wave is always faster than the electrons, a resonant condition occurs such that the radiation slips a distance λ_r relative to the electrons after one undulator period. Thus, under certain favorable conditions, the interaction between the electron beam and the EM wave can be sustained, and a net transfer of energy from electron beam to photon beam occurs. At some distance along the undulator, the radiation generated by the electron beam interacting back on the electron beam induces a periodic modulation of the beam longitudinal density at the radiation wavelength λ_r (microbunching). Because of this density modulation, some fraction of the light being generated within the microbunch is coherent; that is, the amplitude of the electric field in the EM wave is proportional to the number of electrons within the microbunch, making the radiation intensity proportional to the square of the number of electrons. The density modulation leads to a higher radiation intensity, and the higher intensity in turn causes stronger density modulation. The result is an exponential growth in the radiation intensity as well as in the density modulation of the electron beam (Fig. 2). The gain length is the distance over which the power increases by a factor of e (~2.72). Under ideal conditions, this is given by

$$L_G^0 = \frac{\lambda_u}{4\pi\sqrt{3}\rho} \quad (1)$$

where

[1]Advanced Photon Source, Argonne National Laboratory, Argonne, IL 60439, USA. [2]MAX-Laboratory, University of Lund, 221 00 Lund, Sweden. [3]Budker Institute of Nuclear Physics, 630090 Novosibirsk, Russian Federation.

*To whom correspondence should be addressed. E-mail: milton@aps.anl.gov

$$\rho = \left\{ \frac{I}{I_A} \frac{\gamma\lambda_r^2}{16\pi^2\sigma_{trans}^2} \frac{K^2}{(1 + K^2/2)^2} \left[J_0\left(\frac{K^2}{4 + 2K^2}\right) - J_1\left(\frac{K^2}{4 + 2K^2}\right) \right]^2 \right\}^{1/3} \quad (2)$$

is the dimensionless scaling parameter (*5*), I is the peak current of the electron bunch, I_A = 17,045 A is the Alfvén current, $J_{0,1}$ are Bessel functions, and σ_{trans} is the electron bunch transverse root-mean-square (rms) size. The scaling parameter is typically of the order of 0.001 for visible wavelengths and shorter; therefore, the gain length is of the order of 100 undulator periods.

By including the effects of energy spread, angular divergence, and transverse beam size of the electron beam, and also the diffraction of the EM wave, the gain length is increased by a factor $\chi > 1$; that is, $L_G = \chi L_G^0$. The degradation factor χ is small if the electron beam transverse phase space area (the beam size times the angular divergence, called the "emittance") is smaller than the radiation beam phase space area ($\lambda_r/4\pi$), the electron bunch relative energy spread is less than ρ, and if the gain length is less than the radiation Rayleigh length. This degradation factor has been computed for general cases (*24–26*), and the results are summarized in a convenient interpolating formula (*27*).

The phase of the density modulation relative to the radiation field during the exponential growth is such that electrons primarily lose kinetic energy. As the electrons lose energy, however, the phase of the electron motion relative to the EM field changes continuously, and eventually, the phase is such that the electrons start to gain energy back from the EM field. At this point, the growth of the radiation power stops; that is, it saturates (Fig. 2). The radiation power at saturation is roughly given by ρP_b, where P_b is the kinetic power of the electron beam. With degradation effects, it is found empirically (*28*) that the power at saturation is given by $P_s \approx 1.6\rho P_b/\chi^2$. The number of undulator periods required to reach saturation is roughly $N_s \approx \chi/\rho$.

The spectral, and thus temporal, characteristics are somewhat more complicated. If there is monochromatic coherent input radiation with wavelength λ_r (i.e., a seed signal), then the monochromaticity will be preserved (as long as the input signal power is higher than the initial undulator spontaneous radiation power), and the system acts as a coherent amplifier of the seed radiation. In the absence of an input seed signal, the miniscule coherent part of the spontaneous synchrotron radiation is amplified, thus the name "self-amplified spontaneous emission." The noisy startup has a sizable impact on the spectral and temporal characteristics of the output radiation, and these output characteristics will vary from shot to shot.

In SASE, before saturation, the radiation spectrum undergoes a gain-narrowing process in which the spectral width is roughly given by $\Delta\lambda/\lambda_r \approx (\rho/N_u)^{1/2}$, where N_u is the number of the undulator periods traversed. Temporally, the radiation is a superposition of wave trains of coherence length $l_c = \lambda_r^2/\Delta\lambda$, randomly distributed over the length of the electron beam. The relative bandwidth of the radiation at saturation is therefore about ρ, corresponding to a coherence length of about λ_r/ρ. Because of the finite number of distinct longitudinal coherence regions within the EM pulse, there will be an inherent shot-to-shot intensity fluctuation of $1/\sqrt{M}$, where M is the number of coherence regions in the radiation pulse.

Experiment and Analysis

In the LEUTL, there are nine undulators installed along the path of the beam. The undulator period λ_u is 3.3 cm, and the peak on-axis field is 1 T, giving an undulator parameter K of 3.1. Each undulator is 2.4 m in length, and they are separated longitudinally by ~38 cm in order to maintain proper phase matching between undulators while allowing room for diagnostics, a quadrupole magnet, and steering corrector magnets.

Electron beam and optical diagnostics stations are located before the first undulator and after each undulator, for a total of 10 stations. Each station is equipped with electron beam position monitors, charge-coupled device (CCD) cameras, remote filter wheels, and actuators to insert various flags, metallic foils, and mirrors into the bore of the undulator line. A mirror at each station can also direct the SASE light toward a fixed-position high-resolution spectrometer located outside of the tunnel. At the last diagnostics station, following the ninth undulator, an additional mirror can further direct the photon beam to an in-tunnel spectrometer. With this diagnostics suite, we can characterize the signatures of the SASE process—optical power buildup, mode size, radiation spectrum, particle beam microbunching, etc.—as a function of distance along the undulator. Details of the full electron beam and optical measurement suite can be found in (*17*).

Our initial measurements focus on the basic characteristics to confirm saturated SASE operation, e.g., power as a function of distance down the undulator (Fig. 3A). The measured and simulated power gain curves for the beam parameters listed in Table 1 (column A) are plotted. The electron beam energy was 217 MeV, giving an output wavelength of 530 nm. The measured data are normalized to the intensity at the end of the

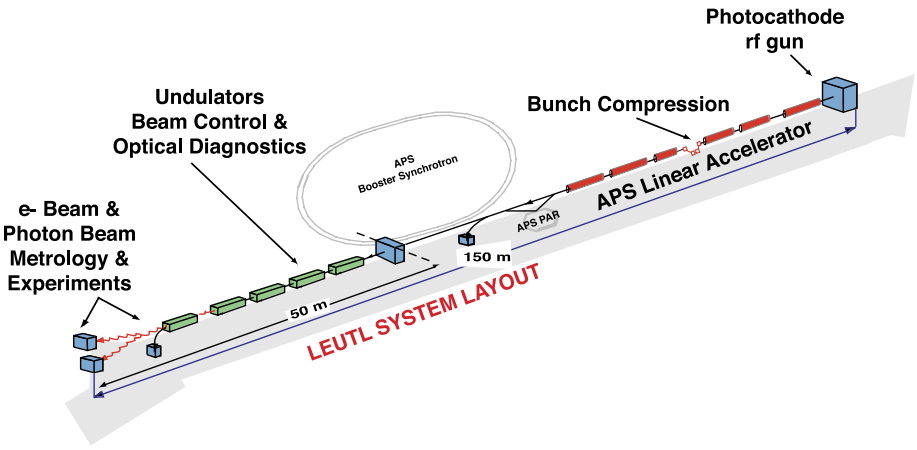

Fig. 1. Schematic of the LEUTL system. The particle accumulator ring (PAR) and booster synchrotron are shown only for reference.

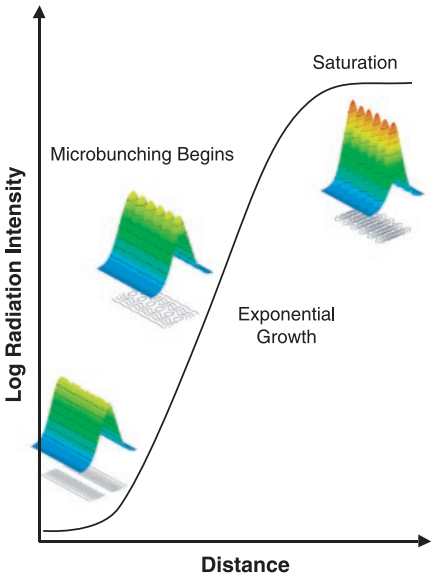

Fig. 2. Schematic representation of the longitudinal microbunching within the colored electron bunch (dark blue, low electron density; red, high electron density) and the exponential growth of the optical signal (solid line) as a function of distance along the undulator. Saturation of the SASE process occurs after ~20 power-gain lengths.

first undulator. The spread is due to both the inherent statistical fluctuation of the SASE process (i.e., the finite number of longitudinal coherence lengths) and fluctuations in the beam properties entering the undulator. Stability of the system was good, as evidenced by the two indistinguishable measured data points at 21.6 m. One was measured at the beginning of the experiment, and the other was measured at the end. Saturation of the SASE process following the seventh undulator (16.8 m) is apparent.

To achieve the observed saturation, we compressed the electron bunch to maximize the peak current. In this situation, the full width at half maximum (FWHM) bunch length (~140 μm) was then shorter than the distance by which the radiation slips ahead of the bunch before reaching saturation (~270 μm in seven undulators). Thus, radiation that slips ahead of the electron bunch stops interacting with the electrons and propagates in free space. The FEL interaction is also very nonuniform across the electron bunch length because the trailing part of the electron bunch experiences less radiation field than the leading part. As a result, the strong slippage effect somewhat reduces the total gain, as well as the saturation level. We simulated this slippage effect with the time-dependent FEL code GINGER (*29*), using the beam parameters listed in Table 1 (column A). Fifty independent SASE runs were made by starting the simulation from random shot noise, and the results were averaged. The simulated radiation pulse energy was normalized to the measured pulse energy following the second undulator. This choice was made because the simulated spectral bandwidth (roughly a few percent and sufficient for SASE) is not sufficient for fully simulating the spontaneous emission following the first undulator. In this short-pulse regime, the saturation level is $\sim 2 \times 10^5$ times that of the pulse energy measured after the first undulator. Very good agreement is found between the experimental data and the simulation. In particular, the gain length (slope) and the location of saturation (at 17 m) are correctly modeled. Table 1 (column A) also lists the calculated gain length obtained from the theoretical interpolating formula (*27*) and from the fit to the experimental data.

To confirm that the energy roll-off seen in Fig. 3A was due to saturation and not to, e.g., defects in the undulators' magnetic fields or beam trajectory problems, we deliberately detuned the electron beam (this was done by increasing the bunch length while maintaining the same charge and thus decreasing the peak current) so as to obtain exponential gain down the entire undulator line without saturation (Fig. 3B). The relevant beam parameters are found in column B of Table 1. The longer bunch length also insured that slippage effects were not an issue and that a more direct comparison of the theoretical intensities to those measured could be made. Stability over time was checked as in Fig. 3A at the 21.6-m data point. The two data points are nearly indistinguishable.

A direct comparison of the experimental and theoretical saturation power levels is hindered because of the lack of an absolute measurement of the radiation pulse energy and the pulse length. Nevertheless, one can make an indirect comparison based on the ratio of the saturated pulse energy to the pulse energy following the first undulator. Assuming the pulse energy at station 1 is mostly spontaneous radiation, we find that the energy radiated into a rms angular cone $\sqrt{\lambda_r/(2N_1\lambda_u)}$ is

$$W_1 = \left[\gamma^2 mc^2 \frac{I}{I_A} \frac{K^2}{(1 + K^2/2)^2} \frac{2\pi^2 c}{\lambda_u}\right] \times \sqrt{2\pi}\sigma_t \quad (3)$$

where N_1 is the number of periods in one undulator and σ_t is the rms bunch duration. Because the local gain is the largest in regions of highest local beam current, the effective radiation pulse length is narrowed

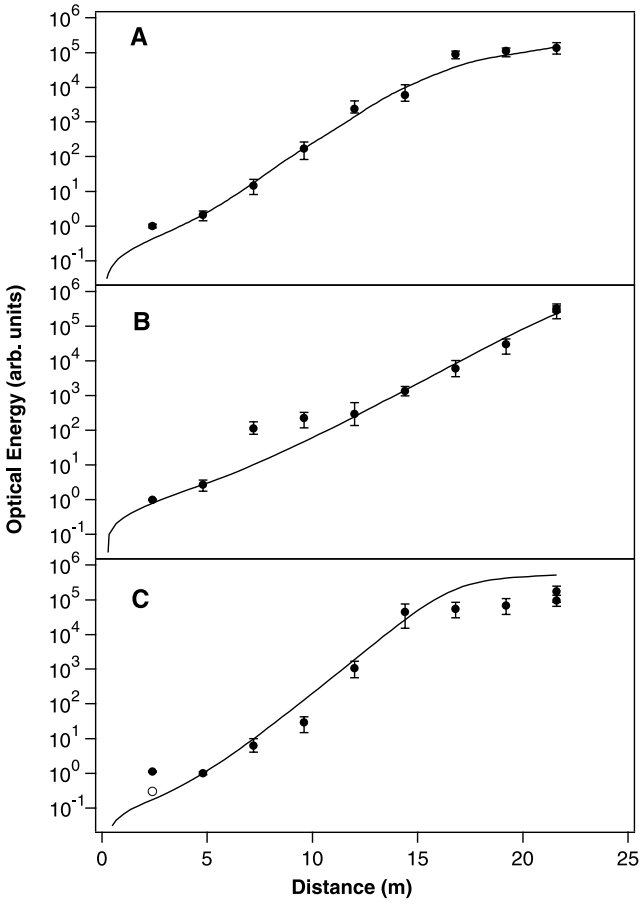

Fig. 3. Optical beam energy (time-integrated power) as a function of distance down the undulator, under various electron beam conditions. (**A**) Table 1, column A, 530-nm saturated conditions. (**B**) Table 1, column B, 530-nm unsaturated conditions. (**C**) Table 1, column C, 385-nm saturated conditions. For the data shown, 100 images were taken at each diagnostic station and used to generate the data points. Images showing evidence of camera saturation were discarded. Plotted are the 25th, 50th (central diamond), and 75th integrated intensity percentiles at each station, with the 25th and 75th connected as a solid line. The solid curves represent GINGER simulation results.

Table 1. Measured beam parameters, measured gain length, calculated gain lengths, and radiation mode properties. Column A shows data from 530-nm saturated conditions, column B shows data from 530-nm unsaturated conditions, and column C shows data from 385-nm saturated conditions.

Parameter	A	B	C
Charge (nC)	0.30 ± 0.02	0.33 ± 0.007	0.30 ± 0.02
rms bunch length (ps)	0.19 ± 0.02	0.77 ± 0.05	0.65 ± 0.05
Peak current (A)	630 ± 78	171 ± 12	184 ± 19
Normalized emittance (π mm · mrad)	8.5 ± 0.9	8.5 ± 1.1	7.1 ± 0.5
rms energy spread (%)	0.4 ± 0.1	0.2 ± 0.1	0.1 ± 0.1
Nominal radiation wavelength (nm)	530	530	385
Measured gain length (m)	0.97	1.4	0.76
Calculated gain length (m)	1.0	1.3	0.80
Calculated FWHM angular divergence (mrad)	0.74	0.62	0.71
Measured FWHM angular divergence (mrad)	0.55 to 1.1	0.76 to 1.2	0.71 to 1.2

relative to the electron pulse. The saturation energy at the saturation distance z_s can be estimated by

$$W_s = P_s\sqrt{2\pi}\sigma_t\sqrt{\frac{L_G}{z_s}} \quad (4)$$

The expected amplification factor from station 1 to saturation is

$$\frac{W_s}{W_1} = \frac{1.6\rho}{\chi^2}\sqrt{\frac{L_G}{z_s}}\frac{\lambda_u(1 + K^2/2)^2}{2\pi^2K^2r_e\gamma_0} \quad (5)$$

where r_e is the classical radius of the electron. Normally, $z_s \approx 20L_G$. With the LEUTL parameters and those of Table 1, this factor is $\sim 10^6$ for all three cases.

The exponential growth of the 530-nm radiation (Fig. 3B) shows an amplification factor of almost six orders of magnitude from the signal level measured after the first undulator to that measured with the last diagnostics station. This is just short of saturation, according to the above argument. Again, the experimental conditions were simulated with the average of 50 runs, and the result is overlaid on the experimental points. With the typical beam parameters listed in Table 1 (column B), the gain length calculated with the interpolating formula also agrees with the experimental result.

In the third set of experiments, the electron beam energy was increased to 255 MeV so that the resonant wavelength was 385 nm. Saturation is again observed (Fig. 3C). The GINGER simulation curve in Fig. 3C was generated with the parameters listed in Table 1 (column C). As for the 530-nm cases, normalization of the radiation energy was performed after the first undulator. Stability over time, although quite good, was not as good as the two previous results. The two separate data points at 21.6 m are clearly distinguishable.

The high intensity measured at the first data point of Fig. 3C can be explained as follows. The transmission curve of the camera lens used for the visible light detectors falls rapidly over the region from 400 to 380 nm. The resonant wavelength is red-shifted when viewed off axis, and this red-shifted radiation was detected by the optical diagnostics. The red-shifted radiation is not amplified by the SASE process. We measure the intensity of SASE light for a given station by integrating the image over a sufficiently large region of the CCD, after a background subtraction. At 385 nm and small SASE power levels, i.e., early on in the SASE process, the red-shifted spontaneous component contributes substantially to the total energy detected, whereas the (non–red-shifted) SASE component is detected with lower efficiency. The open circle in Fig. 3C at 2.4 m is the result of reprocessing the data of the first point using a smaller integration area of the CCD; this area is still large in comparison with the theoretically expected radiation spot size. This reduces the offset caused by the contribution from red-shifted spontaneous radiation while still including the full SASE signal. Reprocessing of the other data points in the same manner has no effect because the SASE signal dominates the signal integration. We show this reprocessed point only as a matter of explanation and do not use it for comparison because its value is dependent on the region of interest, whereas the other points are not.

Once again, comparison of the measured gain length with those derived from simulation and theory are very good (Table 1, column C), and the location at which saturation occurs appears to be close to that predicted by the simulation. However, the saturation power in Fig. 3C is somewhat lower than that predicted by GINGER. This discrepancy may be due to an electron beam trajectory error, small differences in diagnostics transmission in the near-ultraviolet region, the particular choice of simulation parameters, or a combination of these factors.

Further comparison to theory can be made by measurement of the angular divergence of the optical radiation. In the exponential gain regime, the FWHM angular divergence of the guided mode can be estimated by

$$\theta_{FWHM} \approx \sqrt{\frac{\lambda_r}{L_G}} \quad (6)$$

Table 1 lists the calculated divergences and the range of measured divergences in the exponential and saturated regimes. The agreement between theory and experiment is reasonable and within the resolution of the measurement. For the angular divergence measurements (e.g., camera focused at infinity), the typical rms spot size on the camera is in the range of 3 to 4 pixels. Thus, the resolution of this particular measurement is not very high, and subtracting a 1-pixel resolution in quadrature results in much better agreement between the measured and expected results.

Figure 4 shows a series of single-shot spectra, taken after the third (7.2 m), fifth (12 m), and seventh (16.8 m) undulators for the 385-nm conditions. The evolution of the spectrum during the exponential gain region, and near saturation, is clearly apparent. As in any distributed narrowband amplifier, the spectrum narrows before saturation. Near saturation (16.8 m), the relative rms linewidth is $\sim$0.3% and is comparable to the FEL scaling parameter ρ, as expected. Because the coherence time $t_c = \lambda_r^2/(c\Delta\lambda) \approx 0.4$ ps is almost equal to the effective radiation pulse duration $[\sqrt{2\pi}\,\sigma_t\sqrt{L_G/z_s}$ (see Eq. 4)], a single coherence region (mode) appears in the last spectrum.

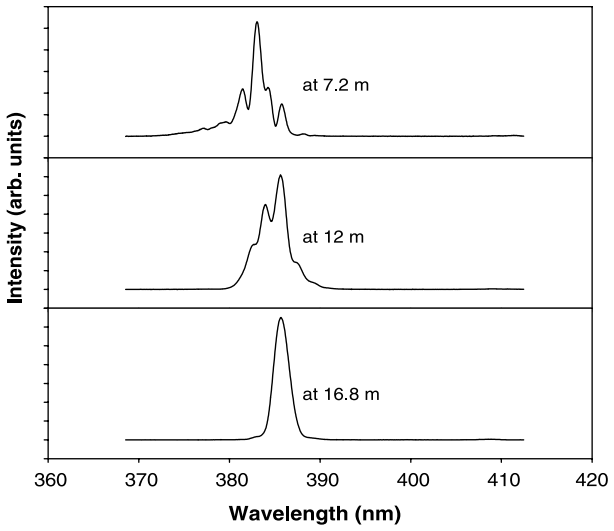

Fig. 4. Single-shot spectra taken at various locations along the undulator line, with the beam tuned for saturation at 385 nm. Spectra were individually normalized to unity.

Conclusion and Summary

SASE with high-quality, high-energy electron beams passed through long, high-quality undulator magnets is seen to be a promising method for achieving unprecedented x-ray brightness. Confirmation of the theory is an essential step toward determining that SASE can reach saturation at short x-ray wavelengths. The study of the SASE process at progressively shorter wavelengths is proceeding rapidly and is being made possible by advances in electron beam generation and control and in magnet technologies. Although beam qualities have not yet reached the requirements for SASE saturation at x-ray wavelengths, we showed that both the electron beam generation techniques and the undulator magnets are of sufficient maturity to reach saturation at ultraviolet wavelengths. We measured the energy (time-integrated power), spectrum, and divergence as a function of length along the undulator system (including start-up, as well as exponential gain to and be-

yond saturation) and found all to be in good agreement with theory. The detailed experimental confirmation of the SASE process and the beam manipulation methodologies required to achieve saturation will continue to improve and move the process to shorter wavelengths, creating the possibility of building a very high brightness, tunable coherent x-ray source.

References and Notes

1. J. L. Laclare, in *Proceedings of the IEEE 1993 Particle Accelerator Conference*, S. T. Coneliassen, Ed. (IEEE, Piscataway, NJ, 1993), pp. 1427–1431.
2. J. N. Galayda, in *Proceedings of the IEEE 1995 Particle Accelerator Conference*, L. Gennari, Ed. (IEEE, Piscataway, NJ, 1995), pp. 4–8.
3. H. Kamitsubo, in *Proceedings of the IEEE 1997 Particle Accelerator Conference*, M. Comyn, M. K. Craddock, M. Reiser, J. Thomson, Eds. (IEEE, Piscataway, NJ, 1997), pp. 6–10.
4. A. M. Kondratenko, E. L. Saldin, *Sov. Phys. Dokl.* **24** (no. 12), 986 (1979).
5. R. Bonifacio, C. Pellegrini, L. M. Narducci, *Opt. Commun.* **50**, 373 (1984).
6. C. Pellegrini, "A 4 to 0.1 nm FEL Based on the SLAC Linac" (Workshop of Fourth Generation Light Sources, Stanford Synchrotron Radiation Laboratory, Stanford, CA, 1992).
7. M. Cornacchia *et al.*, "Linac Coherent Light Source (LCLS) Design Study Report," *Report SLAC-R-521* (Stanford Linear Accelerator Center, Stanford, CA, revised 1998).
8. R. Brinkmann, G. Materlik, J. Rossbach, A. Wagner, Eds., "Conceptual Design of a 500 GeV e^+e^- Linear Collider with Integrated X-Ray Laser Facility," *DESY Report DESY97-048* (Deutsches Elektronen-Synchrotron, Hamburg, 1997).
9. D. A. Kirkpatrick, G. Bekefi, A. C. DiRienzo, H. P. Freund, A. K. Ganguly, *Phys. Fluids B* **1**, 1511 (1989).
10. F. Sakai *et al.*, "Development of High-Duty Operation RF Photoinjector," *Report BNL-65003* (Brookhaven National Laboratory, Upton, NY, 1997).
11. S. G. Biedron *et al.*, in *Proceedings of the IEEE 1999 Particle Accelerator Conference*, A. Luccio, W. Mackay, Eds (IEEE, Piscataway, NJ, 1999), pp. 2024–2026.
12. M. J. Hogan *et al.*, *Phys. Rev. Lett.* **81**, 4867 (1998).
13. M. Babzien *et al.*, *Phys. Rev. E* **57**, 6093 (1998).
14. S. V. Milton *et al.*, *Phys. Rev. Lett.* **85**, 988 (2000).
15. J. Andruszkow *et al.*, *Phys. Rev. Lett.* **85**, 3825 (2000).
16. S. V. Milton *et al.*, *Nucl. Instrum. Methods Phys. Rev. Sect. A* **407**, 210 (1998).
17. S. V. Milton *et al.*, *Proc. SPIE* **3614**, 96 (1999).
18. I. B. Vasserman *et al.*, in *Proceedings of the 1999 Particle Accelerator Conference*, A. Luccio, W. Mackay, Eds. (IEEE, Piscataway, NJ, 1999), pp. 2489–2491.
19. I. B. Vasserman, N. A. Vinokurov, R. J. Dejus, *AIP Conf. Proc.* **521**, 368 (2000).
20. E. Gluskin *et al.*, *Nucl. Instrum. Methods Phys. Rev. Sect. A* **429**, 358 (1999).
21. N. D. Arnold *et al.*, in *Proceedings of the Twenty Second Free-Electron Laser Conference*, V. Litvinenko, Y. Wu, Eds. [*Nucl. Instrum. Methods Phys. Rev. Sect. A* (2000)].
22. G. Travish *et al.*, in *Proceedings of the 20th International Linac Conference*, A. Chao, Ed., SLAC-R-561 (CD available from Stanford Linear Accelerator Center, Stanford, CA, 2000).
23. M. Borland, J. Lewellen, S. Milton, in *Proceedings of the 20th International Linac Conference*, A. Chao, Ed., SLAC-R-561 (CD available from Stanford Linear Accelerator Center, Stanford, CA, 2000).
24. L.-H. Yu, S. Krinsky, R. L. Gluckstern, *Phys. Rev. Lett.* **64**, 3011 (1990).
25. Y. Chin, K.-J. Kim, M. Xie, *Phys. Rev. A* **46**, 6662 (1992).
26. M. Xie, *Nucl. Instrum. Methods Phys. Rev. Sect. A* **445**, 59 (2000).
27. ———, in *Proceedings of the IEEE 1995 Particle Accelerator Conference*, L. Gennari, Ed. (IEEE, Piscataway, NJ, 1995), pp. 183–185.
28. K.-J. Kim, M. Xie, *Nucl. Instrum. Methods Phys. Rev. Sect. A* **331**, 359 (1993).
29. W. Fawley, "An Informal Manual for GINGER and Its Post-processor XPLOTGIN," *BP Tech Note-104* (Lawrence Berkeley National Laboratory, Berkeley, CA, 1995).

30. This work would not have been possible without the outstanding help and dedication of the Advanced Photon Source (APS) technicians, the supporting engineers and scientists, and the management and administrative staff of the APS. In addition, we thank W. Fawley for his help with the simulation code GINGER, P. Emma for many insights into the design of the bunch compressor system, and the people of the Argonne Wakefield Accelerator for the occasional testing of laser and rf equipment. This work is supported by the U.S. Department of Energy, Office of Basic Energy Sciences, under contract W-31-109-ENG-38.

16 February 2001; accepted 20 April 2001
Published online 17 May 2001;
10.1126/science.1059955
Include this information when citing this paper.

G-Protein Signaling Through Tubby Proteins

Sandro Santagata,[1] Titus J. Boggon,[2] Cheryl L. Baird,[4] Carlos A. Gomez,[1] Jin Zhao,[2] Wei Song Shan,[3] David G. Myszka,[4] Lawrence Shapiro[1,2]*

Dysfunction of the tubby protein results in maturity-onset obesity in mice. Tubby has been implicated as a transcription regulator, but details of the molecular mechanism underlying its function remain unclear. Here we show that tubby functions in signal transduction from heterotrimeric GTP-binding protein (G protein)–coupled receptors. Tubby localizes to the plasma membrane by binding phosphatidylinositol 4,5-bisphosphate through its carboxyl terminal "tubby domain." X-ray crystallography reveals the atomic-level basis of this interaction and implicates tubby domains as phosphorylated-phosphatidylinositol binding factors. Receptor-mediated activation of G protein α_q ($G\alpha_q$) releases tubby from the plasma membrane through the action of phospholipase C–β, triggering translocation of tubby to the cell nucleus. The localization of tubby-like protein 3 (TULP3) is similarly regulated. These data suggest that tubby proteins function as membrane-bound transcription regulators that translocate to the nucleus in response to phosphoinositide hydrolysis, providing a direct link between G-protein signaling and the regulation of gene expression.

Obesity has become a severe worldwide epidemic that may soon displace malnutrition as the most significant single factor affecting human health (*1*, *2*). Obesity is a cause of or contributing element in a number of systemic diseases leading to increased risk of mortality. While obesity among the young is a problem of considerable magnitude, adult-onset obesity is a leading cause of decreased life expectancy and is a primary risk factor for type II diabetes, heart disease, and hypertension (*3*, *4*).

The *tubby* strain of obese mice (*5*) provides one of the few defined models for adult-onset obesity. The *tubby* gene, which is highly expressed in the paraventricular nucleus of the hypothalamus and several other brain regions, was identified by isolating the genetic locus that transmits this autosomal recessive obesity syndrome (*6*, *7*). *Tubby* mice have a naturally occurring splice site mutation at the junction of the 3′ coding exon. Targeted deletion of the *tubby* gene results in a phenotype identical to that of the naturally occurring mutant, indicating that the tubby obesity syndrome indeed arises from a loss of function (*8*).

The tubby protein is a member of a homologous family with four members (tubby and TULPs 1 to 3) encoded in the human genome (*9–11*) and with others present in various multicellular organisms (*12*). These proteins feature a characteristic "tubby domain" of about 260 amino acids at the COOH-terminus that forms a unique helix-filled barrel structure; this COOH-terminal domain binds avidly to double-stranded DNA. Mutation of the tubby-like protein 1 gene *TULP1* is the genetic origin of human retinitis pigmentosa type 14 (RP-14) (*12–14*). Mapping mutations from RP-14 patients onto the tubby COOH-terminal domain structure outlines a long, positively charged groove implicated in DNA binding (*15*). Tubby proteins also include NH_2-terminal regions that, in their primary sequence, resemble activation domains from known transcription factors (*15*). Al-

[1]Ruttenberg Cancer Center, [2]Structural Biology Program, Department of Physiology and Biophysics, [3]Department of Biochemistry and Molecular Biology, Mount Sinai School of Medicine of New York University, 1425 Madison Avenue New York, NY 10029, USA. [4]Center for Biomolecular Interaction Analysis, University of Utah, Salt Lake City, UT 84132, USA.

*To whom correspondence should be addressed at the Structural Biology Program, Mount Sinai School of Medicine, Room 16-20, 1425 Madison Avenue, New York, NY 10029, USA. E-mail: shapiro@inka.mssm.edu